American Mineralogist, Volume 85, pages 826–838, 2000

Structure of H-exchanged hexagonal birnessite and its mechanism of formation from Na-rich monoclinic buserite at low pH

BRUNO LANSON,[1,*] VICTOR A. DRITS,[1,2] EWEN SILVESTER,[1,3] AND ALAIN MANCEAU[1]

[1]Environmental Geochemistry Group, LGIT-IRIGM, University of Grenoble—CNRS, 38041 Grenoble Cedex 9, France
[2]Geological Institute, Russian Academy of Sciences, 7 Pyzhevsky Street, 109017 Moscow, Russia
[3]Scientific and Industrial Research for Australia, CSIRO—Division of Minerals, Box 312, Clayton South, 3169, Australia

ABSTRACT

The structural transformation of high pH Na-rich buserite (NaBu) to H-exchanged hexagonal birnessite (HBi) at low pH was studied by simulation of experimental X-ray diffraction patterns. Four HBi samples were prepared by equilibration of NaBu at constant pH in the range pH 5-2. The samples differ from each other by the presence of one (at pH 2 and 3) or two (at pH 4 and 5) phases, and by the structural heterogeneity of these phases which decreases with decreasing pH. The sample obtained at pH 5 is a 4:1 physical mixture of a 1H phase (a = 4.940 Å, $b = a/\sqrt{3}$ = 2.852 Å, c = 7.235 Å, $\beta = 90°$, $\gamma = 90°$) and of a 1M phase (a = 4.940 Å, $b = a/\sqrt{3}$ = 2.852 Å, c = 7.235 Å, $\beta = 119.2°$, $\gamma = 90°$) in which successive layers are shifted with respect to each other by $+a/3$ along the a axis as in chalcophanite. Both the 1H and 1M phases contain very few well-defined stacking faults at pH 5. At pH 4, the sample is a 8:5 physical mixture of a 1H phase containing 15% of monoclinic layer pairs and of a 1M phase containing 40% of orthogonal layer pairs. Any further decrease of the pH leads to the formation of a single defective 1H phase. This 1H phase contains 20% and 5% of monoclinic layer pairs at pH 3 and 2, respectively. Independent of pH, all phases contain 0.833 Mn_{layer} cations, 0.167 vacant layer sites, and 0.167 interlayer Mn cations located either above or below layer vacancies per octahedron. A structural formula is established at each pH.

The origin of the observed phase and structural heterogeneities has been analyzed. 1H and 1M phases are assumed to inherit their specific structural and crystal chemical features from the two distinct NaBu modifications. NaBu type I, with a high proportion of Mn^{4+}_{layer} cations, is thought to be responsible for the monoclinic layer stacking because this configuration allows Mn cations from adjacent layers to be as far as possible from each other, thus minimizing the electrostatic repulsion between these high charge cations. In contrast, NaBu type II has a high interlayer charge induced by Mn^{3+}_{layer} for Mn^{4+}_{layer} substitutions. Consequently, the 1H phase has a high amount of interlayer protons and achieves compensation of the unfavorable overlap of layer and interlayer Mn cations, in projection on the *ab*-plane, by the presence of strong hydrogen bondings between layers. The higher proportion of defined stacking faults in both 1H and 1M phases at pH 4 compared to pH 5 can be attributed to the increase in reaction rate with decreasing pH. At lower pH (3 and 2) the formation of strong hydrogen bonds between adjacent layers controls the layer stacking mode and leads to the formation of a unique 1H phase. The proportion of well-defined stacking faults in this phase decreases from pH 3 to 2.

INTRODUCTION

The phyllomanganates buserite and birnessite both contain layers of edge-sharing Mn-$(O,OH)_6$ octahedra. Buserite has a 10 Å periodicity along the c axis with exchangeable cations and two layers of H_2O molecules in its interlayer space. The partial dehydration of buserite at high pH leads to the formation of 7 Å "monoclinic" birnessite, with a single layer of H_2O molecules. In acidic medium 10 Å buserite converts to 7 Å hexagonal birnessite, in which interlayer Mn cations and protons compensate the layer charge (Burns and Burns 1977, 1978; Chukhrov et al. 1978, 1989; Cornell and Giovanoli 1988). Because of the coexistence of both heterovalent Mn cations and vacant layer octahedra in their structure, buserite and birnessite possess a unique surface charge as well as remarkable redox and cation exchange properties. Cation exchange properties are favored at higher pH, whereas adsorption and redox processes typically occur under low pH conditions. Consequently, these minerals play an essential role in sorption and redox processes in natural environments (McKenzie 1967; Stone and Morgan 1984; Stone and Ulrich 1989; Manceau and Charlet 1992; Stumm 1992; Silvester et al. 1995; Wehrli et al. 1995; Manceau et al. 1997). Because of their contrasting chemical behaviors, it is important to determine their crystal-chemical features at different pH and the mechanism of their structural transforma-

*E-mail: Bruno.Lanson@obs.ujf-grenoble.fr

tion. The distribution of heterovalent Mn_{layer} cations, interlayer cations, and layer vacancies, as well as layer stacking are of special interest in such structural and chemical study. However, a study of minerals from the buserite/birnessite group is difficult because small crystallite size and high density of structural and chemical defects. Consequently, the main structural and chemical characteristics of phyllomanganates are only partly revealed by conventional methods of structural analysis.

Insights into the structural chemistry of synthetic phyllomanganates have been obtained using modern techniques and approaches such as Rietveld refinement (Post and Veblen 1990), powder and polarized EXAFS spectroscopy (Manceau et al. 1992; Silvester et al. 1997; Manceau et al. 1997), simulation of X-ray diffraction (XRD) patterns (Chukhrov et al. 1985; Manceau et al. 1997; Drits et al. 1998), selected area electron diffraction (SAED) (Chukhrov et al. 1978, 1989; Kuma et al. 1994; Drits et al. 1997a, 1998), and solution chemistry (Silvester et al. 1997). These studies have revealed the main features of the structure of birnessite synthesized at different pH, but the nature of structural order-disorder in birnessite prepared at low pH has not been described. The reaction mechanism responsible for the structural conversion of Na-rich 10 Å buserite, synthesized at high pH, into low pH hexagonal H-exchanged 7 Å birnessite also remains poorly understood. From simulation of experimental XRD patterns, the present paper details the actual crystal structural of birnessite samples prepared at pH ranging from 5 to 2, and more especially the atomic coordinates of the different atoms, and the amount of vacant layer sites and of related interlayer cations. Attention is paid to the structural heterogeneity of these samples, and particularly to their layer stacking mode, and the presence and abundance of well-defined stacking faults. Determination of the actual crystal structure of birnessite samples prepared at different low pH conditions has also allowed the refinement, from the structural point of view, of the transformation mechanism of high pH Na-rich buserite into low pH hexagonal birnessite proposed by Silvester et al. (1997).

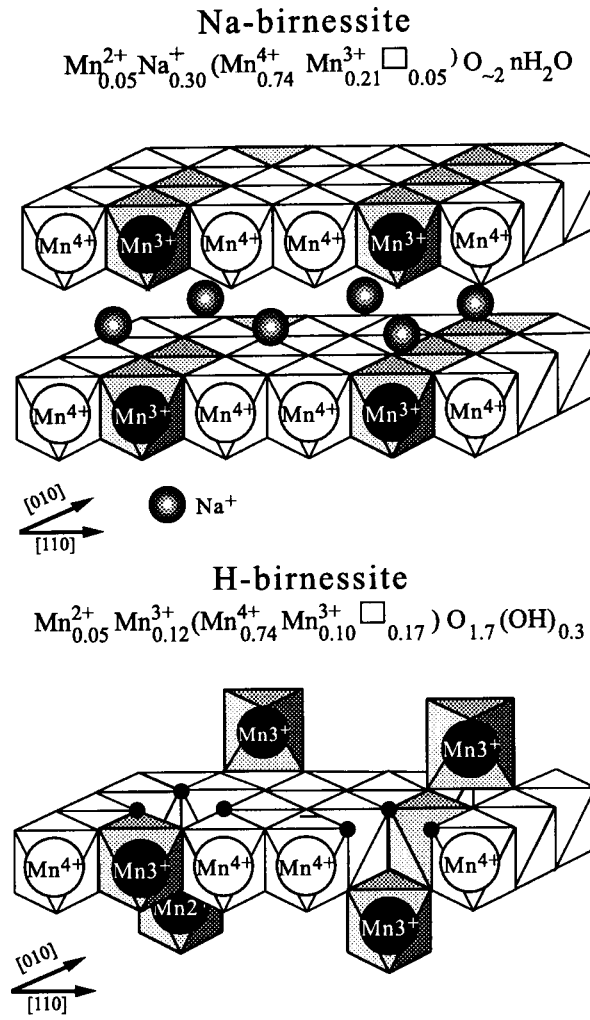

FIGURE 1. Idealized structures of triclinic Na-rich birnessite, and hexagonal H-rich birnessite (pH 4), after Drits et al. (1997a), Silvester et al. (1997), and Lanson et al. (in preparation). Chemical compositions given for NaBu and HBi correspond to averaged values for microcrystals of type I and II. O atoms and water molecules are not shown. (Modified from Manceau et al. 1997)

PREVIOUS STRUCTURAL STUDIES

High pH Na-rich birnessite

The substructure of Na-rich birnessite (NaBi), usually synthesized at very high NaOH concentration ([NaOH] = 2.2 *M*, pH > 14) and equilibrated at high pH (8–10), has a one-layer monoclinic unit cell with an insignificant amount of vacant octahedra (Post and Veblen 1990). Drits et al. (1997a), Silvester et al. (1997), and Lanson et al. (in preparation.) showed that synthetic Na-rich buserite (NaBu) synthesized at high pH consists of vacancy-free layers, and has the composition $Na^{+}_{0.30}(Mn^{4+}_{0.70}Mn^{3+}_{0.30})O_2$ and a one-layer monoclinic unit cell (a = 5.223 Å, b = 2.854 Å, c = 10.265 Å, β = 98.6°; Drits et al. 1998). The partial dehydration of NaBu generates the one-layer triclinic NaBi, with a = 5.169 Å, b = 2.848 Å, c = 7.321 Å, α = 90.8°, β = 103.2°, γ = 90° unit cell, and $Na^{+}_{0.30}(Mn^{4+}_{0.74}Mn^{3+}_{0.21}Mn^{2+}_{0.05})O_2$ composition (Silvester et al. 1997; Lanson et al. in preparation; Fig. 1). NaBi and NaBu contain a considerable proportion of Mn^{3+} which accounts for most of the negative layer charge (Drits et al. 1997a; Lanson et al. in preparation). Further, in both varieties, Mn^{3+} octahedra, distorted by the Jahn-Teller effect, are segregated in Mn^{3+}-rich rows parallel to the b axis and separated from each other along the a axis by two rows of Mn^{4+}. This segregation is responsible for the departure from the hexagonal symmetry of the NaBi layer.

Two NaBi varieties, hereafter referred to as type I and II, are formed during the NaBu-to-NaBi dehydration process, NaBi type II being predominant. These two varieties are differentiated from their Mn^{3+}_{layer} content, which is higher for NaBi type II (Drits et al. 1997a). These contrasting proportions of Mn^{3+}_{layer} lead to different amounts and distributions of Na in the interlayer region of both varieties.

Low pH hexagonal birnessite

This synthetic variety of birnessite, hereafter referred to as HBi, is obtained by the equilibration of NaBu at low pH

(Giovanoli et al. 1970a; Glover 1977; Silvester et al. 1997). HBi is characterized by a 7 Å periodicity along the *c* axis in both humid and air-dried states since its interlayer space contains no hydrated exchangeable cations. HBi has a one-layer hexagonal unit cell with $a = 2.848$ Å, $c = 7.19$ Å, and $\gamma = 120°$ at pH 4 (Drits et al. 1997a). Its layers contain a considerable amount of vacancies with half of the Mn cations initially present in Mn^{3+}-rich rows occupying interlayer sites as a result of disproportionation and migration processes (Manceau et al. 1997). As in the model proposed for NaBu (Drits et al. 1997a) these initial Mn^{3+}-rich rows alternate with two successive Mn^{4+} rows (Fig. 1), the resulting proportion of vacant layer sites in HBi is 1/6 (1/2 cations × 1/3 rows). Interlayer H^+, Mn^{2+}, and Mn^{3+} cations compensate the negative layer charge, with the amount of interlayer Mn^{2+} cations decreasing at lower pH (Silvester et al. 1997).

Mechanism of NaBu-to-HBi conversion

Silvester et al. (1997) and Drits et al. (1997a) proposed that this transformation is a two-step process. The first stage is characterized by rapid exchange of one third of initial $Na^+_{interlayer}$ by solution protons and the disproportionation of one third of the Mn^{3+}_{layer} cations in the Mn^{3+}-rich rows to $Mn^{2+}_{solution}$ and Mn^{4+}_{layer} creating vacant layer sites. During the following slower stage, the remaining $Na^+_{interlayer}$ cations leave the structure and half of the remaining Mn^{3+}_{layer} cations migrate from the layer into the interlayer. At this stage, depending on the solution pH, Mn^{2+} re-adsorbs above or below vacant sites. At pH 5, all desorbed Mn^{2+} (0.05 atoms per unit cell) re-adsorbs whereas at pH 2, no re-adsorption occurs (Silvester et al. 1997). This model is consistent with the transformation from orthogonal to hexagonal layer symmetry as both the disproportionation and the migration of Mn^{3+}_{layer} cations release the steric layer strain originating from the Jahn Teller distortion in the former Mn^{3+}-rich rows.

The partial re-adsorption of Mn^{2+} measured with decreasing pH should result in a decreasing amount of interlayer Mn cations. This conclusion was qualitatively supported by powder EXAFS data (Silvester et al. 1997) which showed that the ratio of layer edge-sharing to interlayer triple corner-sharing Mn-Mn neighbors decreases from pH 2 to pH 5. This result is consistent with an incomplete occupancy of interlayer (above/below layer vacancy) sites at pH lower than 5.

Experimental methods

Experimental methods

Na-rich buserite (NaBu) was synthesized after Giovanoli et al. (1970a). The preparation of low pH birnessite (HBi) was described by Silvester et al. (1997). Four HBi samples were prepared at pH = 5, 4, 3, and 2. Powder XRD patterns were recorded using a Siemens D5000 powder diffractometer equipped with a Cu*K*α radiation. Intensities were measured at an interval of $2\theta = 0.04°$ using a 30 s counting time per step.

Simulation of XRD patterns

As recommended by Drits and Tchoubar (1990) for defective structures, structural information was obtained from the comparison of experimental data with XRD patterns calculated for structural models realistic from a crystal chemistry point of view. The quality of fit was estimated over the 2θ range of 35–65° for Cu*K*α line using the usual R_{wp} parameter. This trial-and-error fitting procedure has been used to determine structural and chemical features of phyllomanganates (Chukhrov et al. 1985; Manceau et al. 1997; Drits et al. 1998; Lanson et al. in preparation). Details of the program used to simulate XRD patterns, and the fitting procedure are given by Drits et al. (1998). Calculation of XRD patterns was limited to 20*l* and 11*l* reflections because these lines are the most sensitive to structural parameters of layered minerals, including order-disorder in their stacking sequences. The background was assumed to be constant over the angular range considered ($2\theta = 30–65°$, Cu*K*α; 2.95–1.45 Å), and no preferred orientation of particles was considered.

Results

Main features of the experimental XRD patterns

The powder XRD patterns of the four samples (Fig. 2) contain an almost rational series of basal reflections and diffraction maxima which were indexed with a one-layer hexagonal unit cell with rather similar parameters (Table 1). However, for later needs, indexing was performed using a base centered unit cell with $a = a_h\sqrt{3}$, $b = b_h$, $\gamma = 90°$. A detailed analysis of these experimental XRD patterns reveals features specific to each HBi samples as a function of the experimental pH conditions.

The shift of experimental *d*-values, from which *a* and *b* parameters were calculated, indicates that *a* and *b* decrease slightly with decreasing pH (Table 1), and although the positions

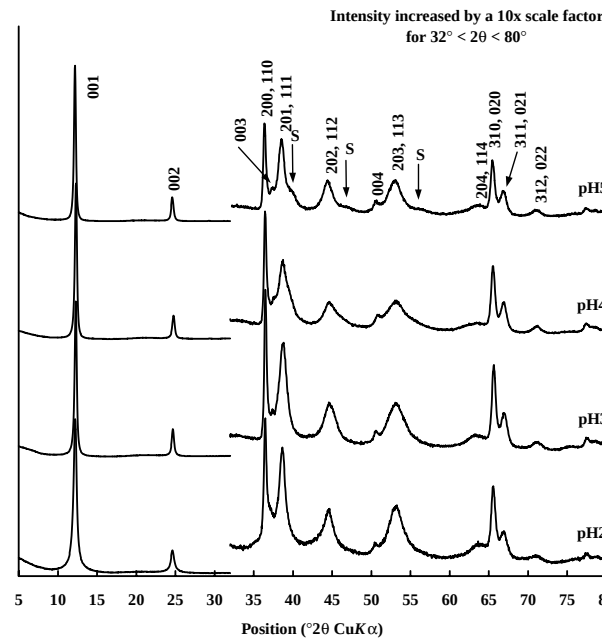

FIGURE 2. Experimental X-ray diffraction pattern of synthetic hexagonal (H^+-exchanged) birnessite obtained by equilibration at low pH of Na-rich buserite. S indicate accessory shoulders of high intensity on the higher 2θ side of 20*l*,11*l* reflections of HBi prepared at pH 5.

TABLE 1. Indexation of the experimental XRD pattern of HBi prepared at different pH

	pH 5		pH 4		pH 3		pH 2	
hkl	*d*(Calc.)	*d*(Exp⁺.)	*d*(Calc.)	*d*(Exp⁺.)	*d*(Calc.)	*d*(Exp.)	Calc.	Exp.
001	7.235	7.265	7.186	7.196	7.213	7.213	7.224	7.248
002	3.618	3.614	3.593	3.593	3.607	3.604	3.612	3.611
200,110	2.470	2.466	2.466	2.461	2.463	2.460	2.464	2.461
003	2.411	2.404 (s)	2.395	2.390 (s)	2.404	2.399 (s)		
201,111	2.337	2.335	2.333	2.326	2.331	2.323	2.332	2.329
202,112	2.040	2.038	2.033	2.029	2.034	2.027	2.035	2.032
004	1.809	1.801	1.797	1.793	1.803	1.803	1.806	1.804
203,113	1.726	1.726	1.718	1.722	1.722	1.722	1.722	1.722
204,114	1.459	1.459 (s)	1.452	1.464 (s)	1.455	1.468 (s)	1.457	1.458 (s)
310,020	1.426	1.424	1.424	1.423	1.422	1.422	1.423	1.423
311,021	1.399	1.398	1.397	1.398	1.395	1.397	1.396	1.397
312,022	1.327	1.326	1.324	1.324	1.323	1.325	1.324	1.325

Notes: The *d* values were calculated using a = 4.940 Å, b = 2.852 Å, c = 7.235 Å, and β = 90° (pH 5), a = 4.933 Å, b = 2.848 Å, c = 7.186 Å, and b = 90° (pH 4), a = 4.926 Å, b = 2.845 Å, c = 7.216 Å, and β = 90° (pH 3), and a = 4.928 Å, b = 2.845 Å, c = 7.224 Å, and β = 90° (pH 2). From the simulation of XRD patterns, the error on a and b parameters may be estimated to ± 0.003 Å and ± 0.002 Å, respectively. (s) indicates a shoulder difficult to index accurately.

of *hkl* reflections are similar for the four samples, each sample has a different reflection profile. At pH = 5, 20*l*,11*l* reflections are relatively sharp and symmetrical although a distinct accessory shoulder is present on the higher 2θ side of each of these reflections (Fig. 2). The 20*l*,11*l* reflections of pH 4 sample are broad and very asymmetrical on the higher 2θ side, but without an accessory shoulder. The symmetry of the 20*l*,11*l* reflection profiles is significantly improved at pH 3, and these reflections become very symmetrical at pH 2. Figure 3 shows that for Cu*K*α an 2θ = 32–42° (2.79–2.15 Å) the background for three samples (pH = 5, 4, and 3) may be considered constant. By contrast, at pH 2 the background starts to increase around 2θ = 34° (2.63 Å) and is higher than for the other three samples. This increase is probably related to the presence of an extremely fine-grained phase formed during the transformation of NaBu at this very low pH. Despite the presence near 2θ = 54.2° (1.69 Å) of another weaker maximum apparently related to this phase, it has been impossible to identify this newly formed product from the positions of these two very broad diffuse maxima (2.45 Å and 1.69 Å). However, this neoformation is reminiscent of the crystallization of nsutite reported by Giovanoli et al. (1970b) during the alteration of Na-buserite at low pH. Nsutite (ICDD no. 17-510) exhibits strong diffraction maxima at 1.64 Å (X), 4.00 Å (9), 2.42 Å (7), and 2.33 Å (7).

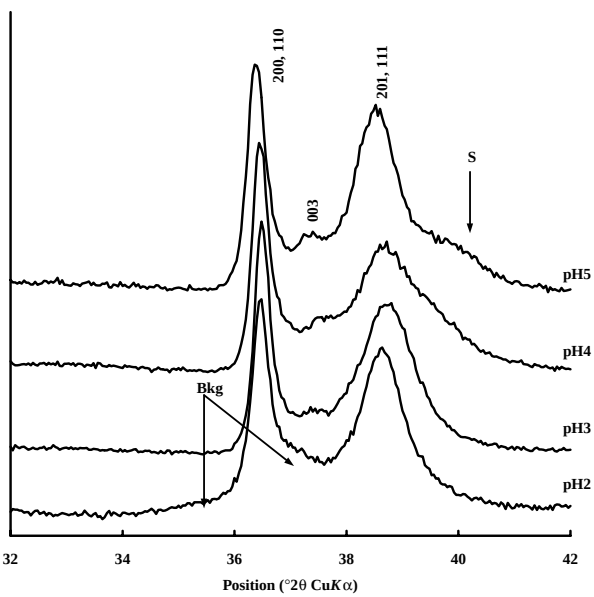

FIGURE 3. Comparison of the relative background intensities for the 4 HBi samples over the 32–42 °2θ Cu*K*α angular range (2.79–2.15 Å). Bkg indicates the significantly increased intensity of background for pH 2, starting around 34 °2θ. S indicates the shoulder on the higher 2θ side of 201,111 reflection of HBi pH 5.

Simulation of the experimental XRD patterns

HBi pH 5. At pH 5, the one-layer hexagonal (1H) structural model for HBi consists of layers containing 0.833 Mn_{layer} atoms and 0.167 vacant sites per octahedron with interlayer Mn cations located either above or below each vacant layer octahedra (Drits et al. 1997a; Silvester et al. 1997, see Fig. 1). In this model, only the z-coordinates of O_{layer} atoms, interlayer Mn cations, and H_2O molecules need to be refined to describe the layer and the interlayer structure, as all other atomic coordinates are deduced from the hexagonal symmetry. Optimum values have been determined by trial-and-error fitting of the experimental XRD pattern (Table 2). Because of the high sensitivity of the intensity distribution to the amount of vacant layer sites and of interlayer cations, these parameters were also adjusted, their optimum value (in both cases 0.167 ± 0.02, see below) being consistent with the initial model. The same approach has been used to determine other adjustable parameters necessary for a complete description of the sample, such as the distribution of coherent scattering domain (CSD) sizes along the *c* axis, the average CSD size along this axis and in the *ab*-plane (Table 3). Figure 4 compares the experimental XRD pattern of HBi pH 5 with the one calculated for 1H structural model free of well-defined stacking faults, hereafter referred to as a defect-free model even though it may contain random stacking faults (See Drits and Tchoubar 1990 for details on well-defined and random stacking faults). All parameters are listed in Tables 2–4, except for the proportion of random stacking faults which was refined to 38% for this model. The relative intensities and the profiles of experimental and calculated 20*l*,11*l* reflections are very similar except for the shoulders which are

TABLE 2. Parameters describing the layer and the interlayer structures for 1H and 1M layer stackings

		Orthogonal layer stacking		Shifted layer stacking	
Mn_{layer}	*x*	0		0	
	y	0		0	
	ζ	0		0	
O_{layer}	*x*	0.333	–0.333	0.333	–0.333
	y	0	0	0	0
	ζ	1.00	–1.00	1.00	–1.00
$Mn_{interlayer}$	*x*	0	0	0	0.333
	y	0	0	0	0
	ζ	2.100	*d*(001) –2.100	2.100	d(001) –2.100
$H_2O_{interlayer}$	*x*	–0.333	0.333	–0.333	0.667
	y	0	0	0	0
	ζ	3.369	*d*(001) –3.369	3.569	d(001) –3.569
c.cos(β)/*a*		+0.000		+0.333	

Notes: These structures are identical regardless of the pH. Optimum values have been determined by trial-and-error fitting of the experimental XRD. As the position of interlayer species associated with the vacant layer sites of the next layer is a function of the shift between adjacent layers, the lower layer is used as a reference to define this position. *x* and *y* coordinates are expressed in fraction of *a* and *b* parameters, respectively. Coordinates along the *c**-axis, *z*, are expressed in Å, to emphasize the thickness of layer and interlayer octahedra.

TABLE 3. Optimum structural parameters to fit the experimental XRD patterns of all four HBi samples (Figs. 7, 8b, 9a, and 10)

	pH 5	pH 4	pH 3	pH 2
a	4.940 Å	4.933 Å	4.926 Å	*a* = 4.928 Å
b	2.852 Å	2.848 Å	2.845 Å	2.845 Å
c	7.235 Å	7.220 Å	7.216 Å	7.224 Å
Mn_{layer} Occ.	0.833	0.833	0.833	0.833
O_{layer} Occ.	1.00	1.00	1.00	1.00
$Mn_{Int.}$ Occ.	0.0833	0.0833	0.0833	0.0833
$H_2O_{int.}$ Occ. 1H	0.32	0.30	0.260	0.260
Additional $H_2O_{int.}$ - x	–	±0.333	±0.333	±0.333
Additional $H_2O_{int.}$ - y	–	0	0	0
Additional $H_2O_{int.}$ - ζ	–	3.610	3.608	3.612
Additional $H_2O_{int.}$ - Occ.	–	0.075	0.125	0.125
Radius of CSD (Å)	130	190	200	150
Mean N	7	7	8	7
Max N	25	28	30	25
W_R	0.26	0.22	0.25	0.28

Note: The parameters describing layer and interlayer structures of 1H and 1M layer stackings are listed in Table 2. Debye-Waller factors were 0.5, 1.0, 1.0, and 1.5 for Mn_{layer}, O_{layer}, Mn_{Int}, and H_2O_{Int} molecules, respectively. Occupancies for O_{layer}, $Mn_{Int.}$, $H_2O_{Int.}$, and additional $H_2O_{int.}$ molecules are given for each of the two symmetrical sites (Table 2), and are thus only half of their actual content per octahedron. Additional $H_2O_{Int.}$ molecules have been introduced only in the orthogonal layer stacking. The radius of the CSD is measured in the *ab*-plane, whereas the coherent scattering domain along the *c**-axis is noted N, and expressed as a number of layers.

not reproduced. It is most likely that these features correspond to an additional HBi variety having a one-layer periodicity along the *c* axis but a monoclinic, rather than hexagonal, unit cell. To check this hypothesis, a set of one-layer monoclinic (1M) models has been considered, all models having the same base-centered orthogonal layer unit cell. The amount and relative positions of vacant layer sites and associated interlayer cations were set as in the 1H phase. The difference between each model was the shift along the *a* axis of successive layers, lowering the symmetry from 1H to 1M. Simulation of XRD patterns corresponding to these models reveals that relative intensities

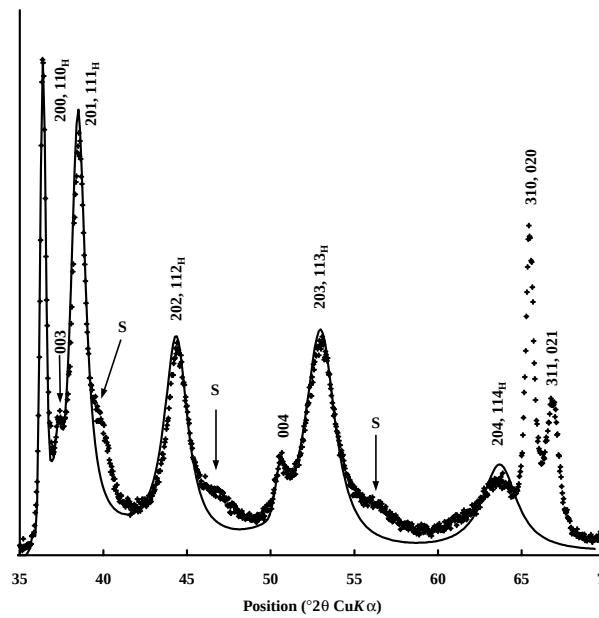

FIGURE 4. Comparison between experimental and calculated XRD patterns for HBi pH 5. Crosses = experimental points. Solid line = the calculated pattern. Only 20*l* and 11*l* lines are calculated. Atomic coordinates and other structural parameters used for the calculation are listed in Tables 2 and 3, except for the proportion of random stacking faults (W_r = 38%). *a* = 4.940 Å, *b* = 2.852 Å, *c* = 7.235 Å, α = β = γ = 90°. S indicate shoulders of high intensity on the higher 2θ side of measured 20*l*,11*l* reflections which are not present in the calculated pattern.

and positions of the shoulders in HBi pH 5 are very similar to those of 20*l* and 11*l* reflections calculated for a model in which successive layers are shifted by + *a*/3 along the *a* axis (Fig. 5). This periodic one-layer monoclinic structure is hereafter referred to as 1M phase. The experimental XRD pattern was reproduced by assuming a 5:1 mixture of 1H and 1M phases, respectively (Fig. 6).

A close examination of 20*l*,11*l* reflections calculated for the 1H phase shows that they are slightly shifted toward lower 2θ values as compared to the experimental peak positions (Fig. 6). This shift may be explained by the diffraction effects described by Drits and McCarty (1996) for the random interstratification of layer fragments having identical thickness but different interlayer displacements. In such cases, the positions of observed *hkl* reflections are located between neighboring *hkl* reflections of phases whose elementary components are interstratified and depend on the relative proportions of these components. As can be seen in Figure 5, experimental $20l,11l_{exp}$ reflections are located between calculated $20l, 11l_H$ and $20l+1, 11\bar{l}_M$ reflections (H and M subscripts refer to 1M and 1H phases, respectively). As a consequence, the positions of the 20*l*,11*l* reflections for a 1H structure containing layers shifted, with respect to the previous one, by +*a*/3 along the *a* axis should be shifted toward higher 2θ values in comparison with a defect-free 1H structure (Figs. 4 and 6). Accordingly, the best agreement between experimental and calculated XRD patterns was obtained for a defective 1H structure containing 8% of such shifted layers. Figure 7 shows the best fit (R_{wp} = 8.40%) obtained for a 4:1 physical mixture of this defective 1H structure and of the defect-free 1M phase. Structural parameters of the two phases are listed in Tables 2–4. By comparing the simulated XRD patterns shown on Figures 6 and 7, one may deduce that the estimated error on the proportion of well-defined 1M stacking faults in the predominant 1H phase is lower than 5%.

HBi pH 4. At pH 4, it was impossible to obtain a good agreement between the experimental trace and XRD patterns calculated using the model obtained for HBi pH 5, since the $20.l+1,11\bar{l}_M$ reflections corresponding to the defect-free 1M phase are shifted as compared to the positions of the asymmetry observed on the higher 2θ side of $20l,11l_H$ reflections (Fig. 8a). This shift is most likely related to interstratification effects similar to those described for the 1H phase at pH 5. Because of the respective positions of $20l,11l_H$ and $20.l+1,11\bar{l}_M$ reflections, the introduction of layer pairs having orthogonal stacking in the 1M structure should lead to the reflection displacement observed experimentally. Accordingly, the best agreement between experimental and calculated XRD profiles (Fig. 8b, R_{wp} = 7.82%) was obtained for a model consisting of a 8:5 physical mixture of the prevailing 1H phase containing 15% monoclinic layer pairs (Table 4) and of the 1M model containing 40% of orthogonal layer pairs, respectively. In both phases, orthogonal and monoclinic layer pairs were found to be randomly interstratified. According to Silvester et al. (1997), at pH 4 HBi was expected to contain 0.156 interlayer cation per octahedron as a consequence of the incomplete re-adsorption of Mn^{2+}. The same quality of fit was obtained with 0.167 (Fig. 8b, R_{wp} = 7.82%) and for 0.156 (R_{wp} = 7.68%) interlayer Mn cation per octahedron because this difference is within the accuracy of the method (±0.02, see below).

HBi pH 3. The improved symmetry of the 20*l*,11*l* reflec-

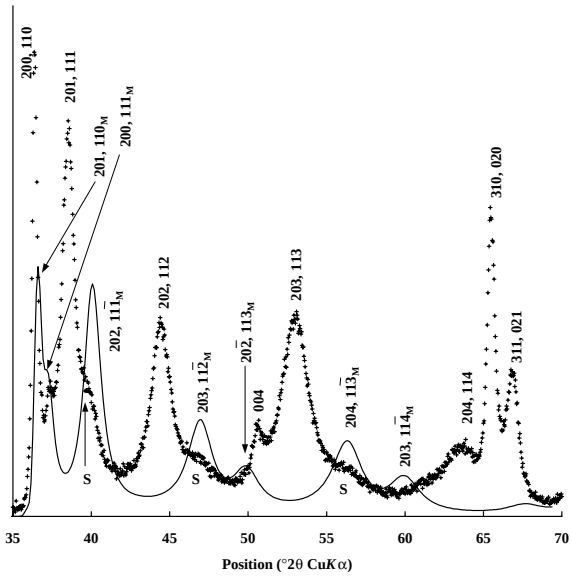

FIGURE 5. Comparison between experimental and calculated XRD patterns for HBi pH 5. 20*l*,11*l* reflections are calculated for a model in which successive layers are shifted by + *a*/3 along the *a* axis with respect to each other. All other structural parameters are similar to those used for Figure 4. The M indices refer to the calculated monoclinic (1M) pattern. Patterns as for Figure 4.

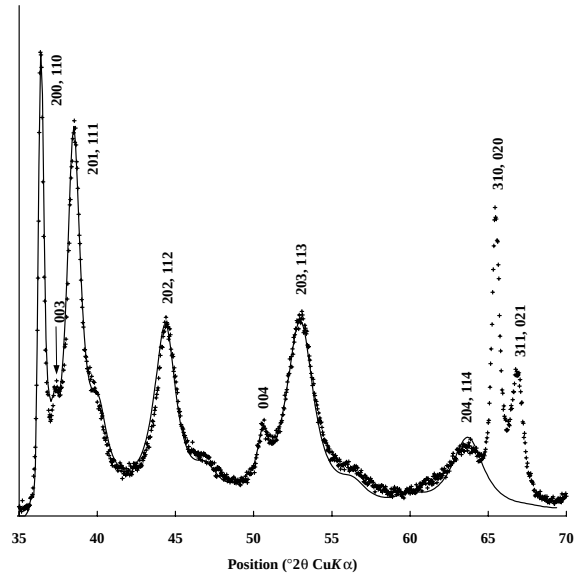

FIGURE 6. Comparison between experimental and calculated XRD patterns for HBi pH 5. The calculated pattern is a 5:1 physical mixture of 1H and 1M phases, whose patterns are shown in Figures 4 and 5, respectively. Patterns as for Figure 4.

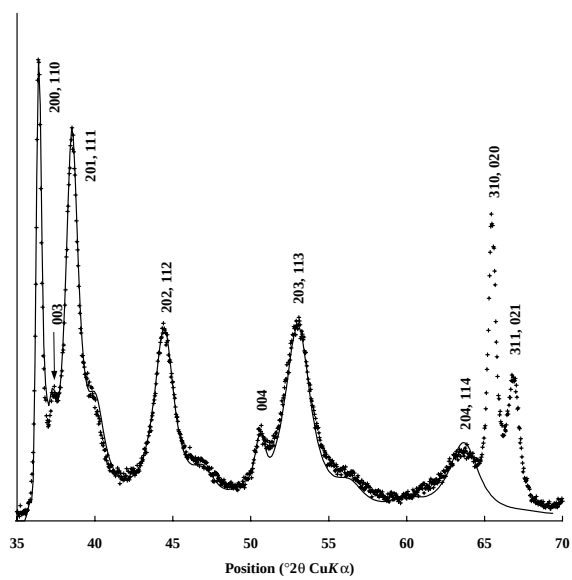

FIGURE 7. Comparison between experimental and calculated XRD patterns for HBi pH 5. The optimum agreement is a 4:1 physical mixture of a defective 1H phase and of a defect-free 1M phase. The defective 1H phase is a random interstratification of 92% of orthogonal layer pairs with 8% of monoclinic layer pairs. The defect-free 1M phase is identical to Figure 5. All other structural parameters are listed in Tables 2 and 3. Patterns as for Figure 4.

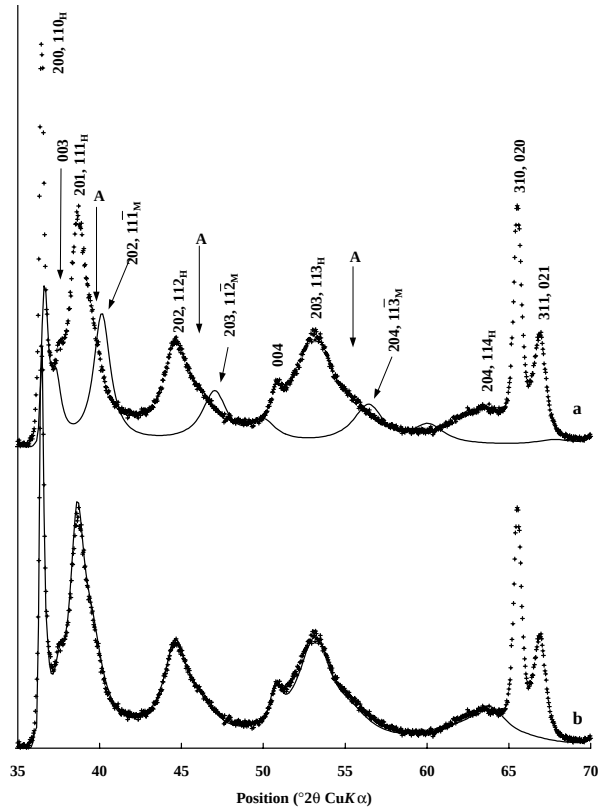

FIGURE 8. Comparison between experimental and calculated XRD patterns for HBi pH 4. (**a**) Defect-free 1M phase in which successive layers are shifted by + *a*/3 along the *a* axis with respect to each other. All other structural parameters are similar to those listed in Tables 2 and 3 for the defective 1M phase. A indicate accessory shoulders on the higher 2θ side of 20*l*,11*l* reflections. (**b**) The optimum agreement is a 8:5 physical mixture of defective 1H and 1M phases. The defective 1H phase is a random interstratification of 85% of orthogonal layer pairs with 15% of monoclinic layer pairs, whereas defective 1M phase is a random interstratification of 60% of monoclinic layer pairs with 40% of orthogonal layer pairs. All other structural parameters are listed in Tables 2 and 3. Patterns as for Figure 4.

tions observed experimentally at pH 3 was found to be related to the significant increase in the proportion of orthogonal layer pairs and, as a consequence, to the formation of a single defective 1H phase containing 20% of monoclinic layer pairs (Fig. 9a; Table 4; R_{wp} = 8.97%). As for the pH 5 and 4 samples, this optimum fit was obtained for 0.167 layer vacancies and interlayer Mn cations for the two layer types. A significant disagreement between experimental and calculated distributions of intensities was observed when the amount of interlayer Mn cations was fixed to the value of 0.134 calculated by Silvester et al. (1997) from solution chemistry data. The discrepancy is stronger if the amount of vacant layer sites per octahedron remains equal to 0.167 (Fig. 9b, R_{wp} = 12.52%), as suggested by Silvester et al. (1997), than if this amount is decreased to 0.134 (Fig. 9c, R_{wp} = 10.29%). The amount of interlayer cation is estimated with an accuracy better than ±0.02 cation per layer octahedron, as shown previously by Manceau et al. (1997) for Co-containing birnessites equilibrated at low pH. Because of this high sensitivity of calculated reflection intensities and profiles to layer vacancy and interlayer cation contents, the values determined for these crystal-chemical characteristics may be considered very reliable, at least for the predominant 1H phase.

HBi pH 2. The increased intensity of the diffuse background near 200,110 and 201,111 reflections observed at pH 2 is believed to result from the partial dissolution of NaBu and the subsequent precipitation of an unidentified phase at this low pH. The newly formed phase has not been identified because it gives

TABLE 4. Optimum structural parameters to fit the experimental XRD patterns of all four HBi samples (Figs. 7, 8b, 9a, and 10)

	pH 5	pH 4	pH 3	pH 2
Proportion of 1H phase	80%	60%	100%	100%
Proportion of 1M phase	20%	40%	0%	0%
Prop. of 1M stacking faults in 1H phase	8%	15%	20%	5%
Prop. of 1H stacking faults in 1M phase	0%	40%	–	–

Note: In all samples, the interstratification of 1M and 1H layer pairs is random, in both 1M and 1H phases, the occurrence probability of two successive 1M or 1H layer pairs being always equal to the relative proportion of 1M and 1H layer pairs, respectively, in the considered structure.

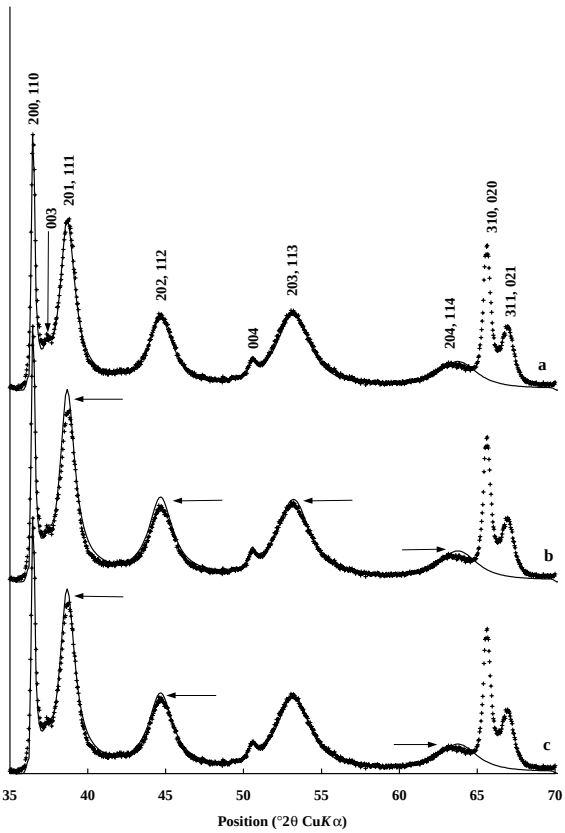

FIGURE 9. Comparison between experimental and calculated XRD patterns for HBi pH 3. (**a**) The optimum agreement is a defective 1H phase which is a slightly segregated interstratification of 80% of orthogonal layer pairs with 20% of monoclinic layer pairs. All other structural parameters are listed in Tables 2 and 3. (**b**) Influence of the interlayer cation site occupancy on the distribution of intensity for calculated XRD profiles. Major discrepancies are indicated by arrows. Site occupancy is lowered to 0.134 according to the model proposed by Silvester et al. (1997) instead of 0.167 for the optimum agreement (Tables 2 and 3 Fig. 9a). All other structural parameters are identical to those used for the optimum agreement. (**c**) Influence of the cation layer and interlayer site occupancy on the distribution of intensity for calculated XRD profiles. Major discrepancies are indicated by arrows. Interlayer site occupancy is lowered to 0.134, together with the amount of layer vacancies, instead of 0.167 for the optimum agreement (Tables 2 and 3; Fig. 9a). All other structural parameters are identical to those used for the optimum agreement. Patterns as for Figure 4.

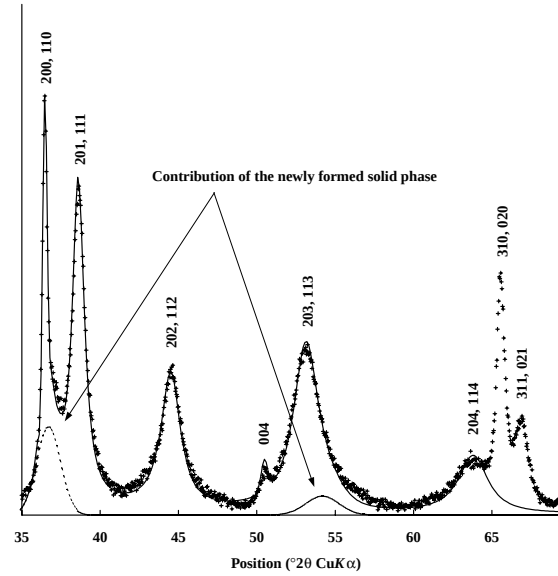

FIGURE 10. Comparison between experimental and calculated XRD patterns for HBi pH 2. The optimum agreement is obtained for a defective 1H phase which is a random interstratification of 95% of orthogonal layer pairs with 5% of monoclinic layer pairs. All other structural parameters are listed in Tables 2 and 3. Patterns as for Figure 4.

only two visible diffuse maxima around 36.7 and 54.2°2θ Cu$K\alpha$ (2.45 and 1.69 Å, respectively) in the experimental XRD pattern. When taking into account the contribution of this poorly crystallized phase, a good agreement between experimental and calculated XRD patterns (R_{wp} = 8.22%) was obtained for a unique HBi phase corresponding to a defective 1H structure containing 5% of monoclinic layer pairs (Fig. 10; Table 4). It should be emphasized that this fit was obtained using 0.167 vacant layer sites and interlayer Mn cations per octahedron, and that the pattern calculated using 0.111 interlayer Mn cations, as suggested by Silvester et al. (1997), differs significantly from the experimental one (R_{wp} = 10.74%; data not shown).

DISCUSSION

Phase and structural heterogeneity of HBi

Experimental XRD patterns of the various samples differ from each other by the profiles and the positions of their diffraction maxima. Simulation of XRD patterns showed, on the one hand, that the shoulders observed for samples equilibrated at pH 5-4 result from the presence of an accessory 1M phase coexisting with the main 1H phase. On the other hand, the position of the diffraction maxima is a function of the structural heterogeneity of these phases, and in particular of the interstratification of 1M and 1H structural fragments within a given phase. Both phase and structural heterogeneities depend on the pH and decrease from pH 5 to pH 2 (Table 4). Throughout the pH 5-2 range, structural and crystal-chemical characteristics of the 1H phase remain about constant, with this prevailing phase containing no more than 20% of monoclinic stacking faults. Conversely, the second phase (1M) is very sensitive to the equilibration pH.

The phase heterogeneity observed in HBi equilibrated at pH 5 may be related to the structural heterogeneity of high pH NaBi which is a physical mixture of two types of crystallites with contrasting layer charges (Drits et al. 1997a). If the coexistence of NaBi type I and II logically results from the presence of two distinct phases in the initial NaBu, one may also expect the presence of two phases in HBi pH 5. Because at pH 5, the 4:1 ratio between 1H and 1M phases (Table 4) is identical to the 4:1 ratio between NaBi crystallites type II and I (Drits et al. 1997a; Silvester et al. 1997; Lanson et al. in preparation), the 1H and

1M phases may be considered as the respective transformation products of NaBu type II and I crystals. Consequently, the main structural features of 1H and 1M interlayer regions will be considered to determine the factors responsible for the structural control of the initial NaBu variety on the stacking mode of 1H and 1M HBi phases. It is important to note that this control is preserved only in slightly acidic conditions (pH 5).

Structural features of the 1H phase

According to Drits et al. (1997a) the composition of NaBu type II is $Na^{+}_{0.333}(Mn^{4+}_{0.667}Mn^{3+}_{0.333})O_2$, and upon lowering the pH there is a significant migration of Mn^{2+} and Mn^{3+} cations into the interlayer of HBi (Silvester et al. 1997). So that vacant layer sites form in the initial Mn^{3+}-rich rows (Fig. 1). Within these rows, 0.055 vacant layer sites (1/6 sites × 1/3 rows) are formed per octahedron as a result of the disproportionation of Mn^{3+} according to the reaction $Mn^{3+}_{layer} + Mn^{3+}_{layer} \rightarrow Mn^{4+}_{layer} + Mn^{2+}_{interlayer} + \square_{layer}$, where $\square_{layer}$ represents a vacant layer site (Silvester et al. 1997). Additionally, half of the Mn^{3+} cations remaining in these former Mn^{3+}-rich rows after the initial disproportionation migrate either above or below newly formed vacant layer sites. Concurrently, interlayer Na^{+} cations are exchanged by H^{+}, yielding the structural formula proposed by Manceau et al. (1997) for 1H HBi at pH 5 $H^{+}_{0.33}Mn^{3+}_{0.111}Mn^{2+}_{0.055}(Mn^{4+}_{0.722}Mn^{3+}_{0.111}\square_{0.167})O_2$.

Consequently, an essential feature of 1H HBi is its high negative layer charge (0.778 = 0.111 + 4 × 0.167 per octahedron), compensated by the presence of interlayer Mn^{3+}, Mn^{2+}, and H^{+} cations, the high amount of $H^{+}_{interlayer}$ resulting from the replacement of $Na^{+}_{interlayer}$ in initial NaBu. Along former Mn^{3+}-rich rows, occupied and vacant layer sites alternate regularly (Drits et al. 1997a) to create a specific distribution of undersaturated O_{layer} atoms (Fig. 11). The three O atoms forming the roof of an empty octahedron (in Fig. 11) are coordinated to only two Mn_{layer} cations. Assuming non-distorted layer octahedra, each of these O atoms receives approximatly 0.500 + 0.667 = 1.167 positive charge if coordinated to Mn^{3+} and Mn^{4+} (open circles), or 0.667 + 0.667 = 1.333 positive charge if coordinated to two Mn^{4+} (half-and-half circles). In both cases, these three O atoms are strongly undersaturated as, globally, they receive only 3.667 (2 × 1.167 + 1.333) or 3.833 (1.167 + 2 ×

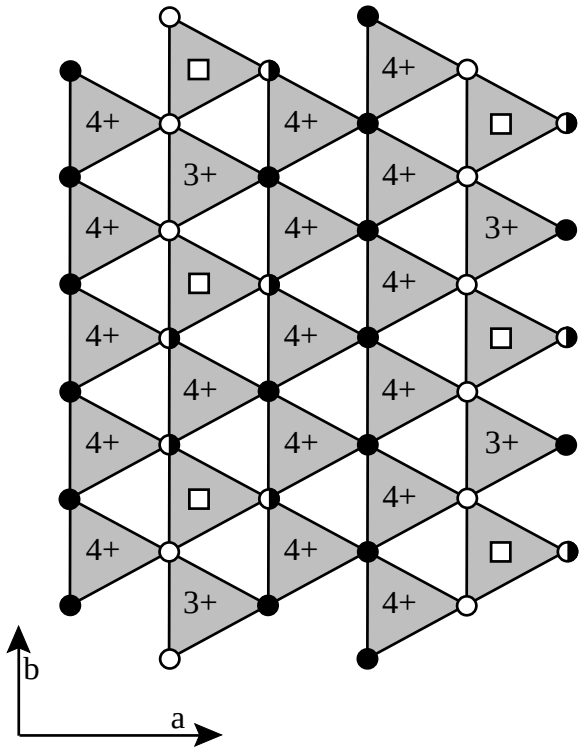

FIGURE 11. Idealized structural model for the 1H phase of HBi. Distribution of undersaturated O_{layer} atoms within the upper surface of the lower layer (grey triangles) in projection on the *ab*-plane. Mn^{3+}_{layer}, Mn^{4+}_{layer} atoms, and vacant layer sites are shown as 3+, 4+, and open squares, respectively. Large circles = O atoms forming the upper surface of the lower layer. Solid circles = saturated or almost saturated O_{layer} atoms. Split circles = unsaturated O_{layer} atoms coordinated to 2 Mn^{4+}_{layer} atoms. Open circles = most undersaturated O_{layer} atoms coordinated to 1 Mn^{4+}_{layer} and to 1 Mn^{3+}_{layer}. Interlayer Mn cations are not shown.

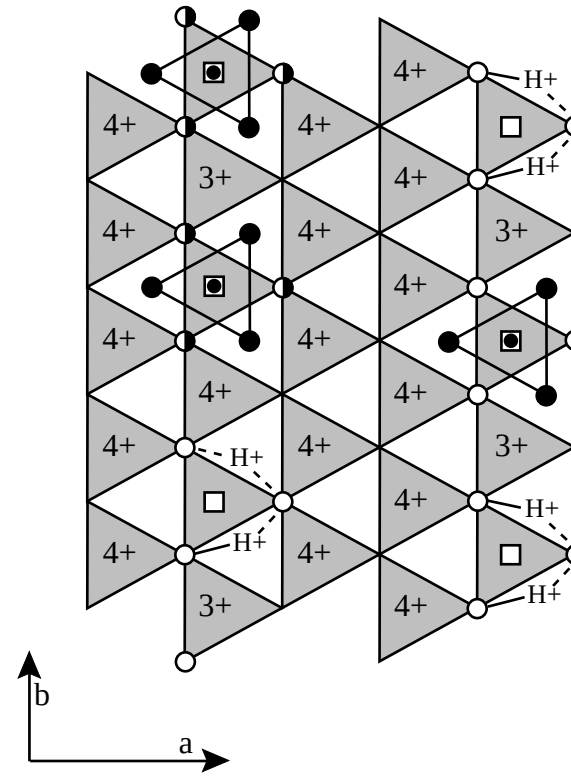

FIGURE 12. Possible distribution in projection on the *ab*-plane of protons within the interlayer region of the 1H phase. Small solid circles = Interlayer Mn cations. Large solid circles = H_2O molecules coordinating these cations. Saturated or almost saturated O_{layer} atoms are not shown. Large split circles = O_{layer} atoms saturated by the presence of interlayer Mn atoms. Large open circles = Undersaturated O_{layer} atoms are shown as. Possible positions of protons (2 per vacant layer site) are shown as H^{+}. Their interactions with O_{layer} atoms are indicated by solid and dashed lines for strong and weak/medium interactions, respectively.

1.333) positive charges, requiring two positive charges on each side of a vacant layer site to achieve local charge balance (two protons on one side, and one Mn^{2+} cation or one $(Mn^{III}OH)^{2+}$ on the other). In the latter case, one H_2O molecule is dissociated into H^+ and $(OH)^-$ to permit this local charge compensation. Even though we do not know the exact distribution and bondings of the protons, it is likely that they are close to the undersaturated O atoms and most probably bound to them. One possible distribution of these protons is shown in Figure 12 where they are predominantly bound to the most undersaturated O atoms, i.e., those coordinated to one Mn^{3+} and one Mn^{4+} atoms (solid lines), and interact to a lesser extent with the O atoms coordinated to two Mn^{4+} (dashed lines).

On the opposite side of vacant sites, even the coordination of the O atoms forming the roof of such sites by interlayer Mn^{3+} and Mn^{2+} cations leaves them undersaturated, as the sum of positive charges they receive ranges from 1.667 (1.167 + 0.500) to 1.833 (1.333 + 0.500) if Mn^{3+} is the interlayer cation, and from 1.500 (1.167 + 0.333) to 1.667 (1.333 + 0.333) if Mn^{2+} is the interlayer cation. Therefore, to increase their saturation by positive charge, $Mn^{2+,\,3+}_{interlayer}$ should migrate toward these anions along the *c* axis, thus increasing the bond strength (Brown 1981, 1992). The remainder of $Mn^{2+,\,3+}_{interlayer}$ positive charges is shared with $H_2O_{interlayer}$ coordinated to these cations. Figure 13 shows such an idealized model of 1H HBi interlayer structure. Here, the three $H_2O_{interlayer}$ coordinating $Mn_{interlayer}$ cations form an empty prism with the three O_{layer} of the adjacent octahedron of the adjacent layer. Because it provides short O_{layer}-$H_2O_{interlayer}$ distances (2.82-2.87 Å), the orthogonal layer stacking provides an optimum configuration to form H-bonds between the O_{layer} of a vacant octahedron and $H_2O_{interlayer}$ coordinating $Mn_{interlayer}$ of the adjacent layer. Consequently, this layer stacking is favored in a phase having a high negative layer charge, because this charge is compensated by a large amount of interlayer manganese cations and protons. Finally, both the high negative layer charge and the abundance of interlayer cations may be considered as essential factors for the formation of the 1H structure as a result of the low pH transformation of NaBu type II.

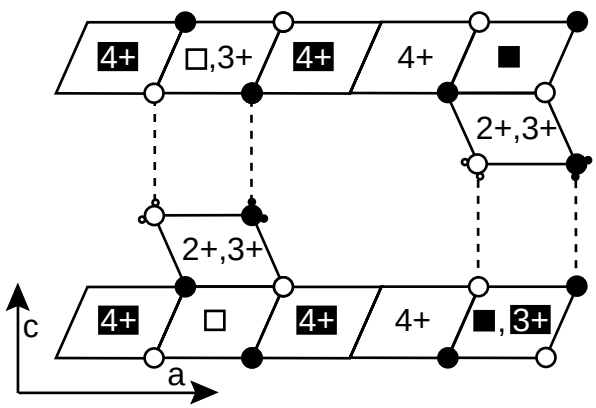

FIGURE 13. Idealized structural model for the 1H phase of HBi. Projection of the layer and interlayer structures of the 1H phase along the *b* axis. Interlayer Mn cations are shown as 2+, 3+, whereas $Mn^{4+}{}_{layer}$ and vacant layer sites are shown as 4+ and squares, respectively. Large circles = O atoms. Saturated O_{layer} atoms and protons are not shown. Open symbols indicate atoms at $y = 0$, and solid symbols indicate atoms at $y = \pm 1/2$. The prisms defined by very undersaturated O_{layer} atoms and H_2O molecules coordinated to interlayer Mn cations are outlined by dashed lines. These dashed lines also indicate possible H-bonds between these two species.

Structural features of the 1M phase

To determine the factors responsible for the structural control of NaBu type I on the stacking mode of the 1M phase it is necessary to consider the differing contents of high valency Mn cations between NaBu type I and II. According to Drits et al. (1997a) NaBu type I composition could vary from $Na^+_{0.167}(Mn^{4+}_{0.833}Mn^{3+}_{0.167})O_2$ to $Na^+_{0.25}(Mn^{4+}_{0.75}Mn^{3+}_{0.25})O_2$, as compared to $Na^+_{0.333}(Mn^{4+}_{0.667}Mn^{3+}_{0.333})O_2$ for NaBu type II. If one assumes that the negative layer charge of NaBu type I is 0.20 per octahedron, and that the 1M phase results from the low pH transformation, without disproportionation, of NaBu type I, then the idealized structural formula of the 1M phase should be $H^+_{0.333}Mn^{3+}_{0.167}(Mn^{3+}_{0.80}Mn^{3+}_{0.033}\square_{0.167})O_2(OH)^-_{0.133}\cdot(H_2O)_{0.367}$, if only H_2O molecules from the hydration sphere of $Mn_{interlayer}$ cations are considered. The higher proportion of high valency Mn cations in this 1M phase, as compared to the 1H phase, is assumed to be responsible for its stacking mode.

Because of the $+a/3$ displacement along the *a* axis between adjacent layers, the structure of this phase is indeed similar to the 3R structure of chalcophanite (Post and Appleman 1988) and is characterized by the same AbC b'A'c' BcA c'B'a' CaB a'C'b' AbC stacking sequence (A, B, and C represents O_{layer} sites, A', B', and C' sites for H_2O molecules and OH groups, a, b, and c Mn_{layer} sites, and a', b', and c' $Mn_{interlayer}$ sites). The projection of such a 1M structure along the *b* axis is shown in Figure 14. In this structure, distances between Mn_{layer} cations of adjacent layers as well as between $Mn_{interlayer}$ cations of one layer and Mn_{layer} of the adjacent one are maximized. Consequently, the electrostatic interactions between these high valency Mn cations is minimized for such a $+a/3$ interlayer displacement of adjacent layers along the *a* axis. Even though the location of $Mn_{interlayer}$ is identical in both 1M and 1H phases, the main difference between these phases is the structure of the interlayer resulting from different interlayer displacements. In 1M HBi, as in chalcophanite, $H_2O_{interlayer}$ form empty octahedra with the O_{layer} of the adjacent layer (Fig. 14), and O_{layer}-H_2O distances (3.10-3.15 Å) are longer than those in the 1H phase (2.82-2.87 Å). As a result, hydrogen bonding is much weaker in the 1M phase than in the 1H phase, and one may consider that in the 1M phase the stacking sequence is mainly controlled by the minimization of the electrostatic repulsion between high valency Mn cations from adjacent layers.

Structural transformation of NaBu to HBi as a function of pH

As shown above, at least two structural factors, the formation of hydrogen bondings and the minimization of cation electrostatic interaction, are likely responsible for the different layer stackings observed in HBi. In particular, the abundance of high-valency Mn cations in the layers of NaBu type I predetermines the monoclinic layer stacking of the 1M phase, thus minimizing the cation electrostatic repulsion between adjacent layers.

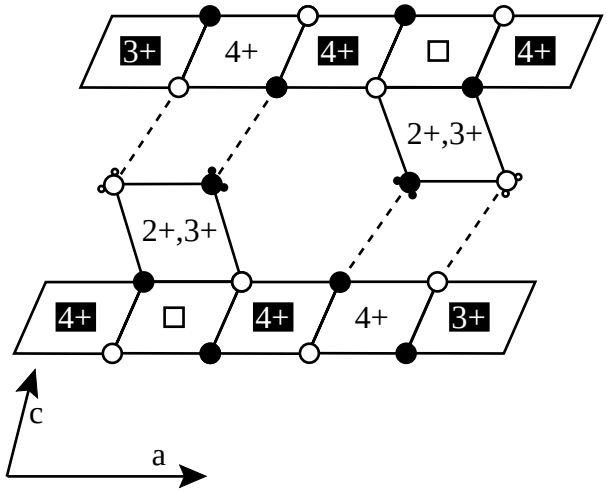

FIGURE 14. Idealized structural model for the 1M phase of HBi. Projection of the layer and interlayer structures of the 1M phase along the *b* axis. All symbols as in Figure 13. Dashed lines indicate the vacant interlayer octahedra defined by very undersaturated O_{layer} atoms and H_2O molecules coordinated to interlayer Mn cations. The edges of these octahedra are too long to permit H-bonds.

Similarly, the high negative layer charge of NaBu type II, which is compensated by interlayer cations, is responsible for the orthogonal layer stacking of the 1H phase, in spite of the unfavorable manganese cation configuration. In this case, the cation repulsion is compensated by the formation of strong hydrogen bondings between adjacent layers, providing the maximum stability possible to these layer pairs. The 1M phase may be considered metastable because the weaker interlayer bonding permits its transformation to the stable orthogonal layer stacking as a result of the increasing amount of available protons when decreasing the pH. At lower pH, the physico-chemical conditions, rather than the structure of the precursor phase, controls the stacking mode. The presence of the 1M phase at pH 4 and 5 is most likely related to the lower probability of overcoming the energy barrier to the direct formation of the 1H phase in slightly acidic conditions because of the lower amount of available protons. This hypothesis is supported by the longer-lasting H^+ consumption observed at pH 5 (~40 hours) than at pH 2 (a few minutes). However, along with these crystal-chemical factors, the reaction rate may also play an essential role in the structural transformation.

To understand the possible influence of the reaction rate it is necessary to consider the layer displacements responsible for the structural transformation. In the idealized structures of NaBi (Post and Veblen 1990; Lanson et al. in preparation.) and NaBu (Lanson unpublished data), adjacent layers are shifted with respect to each other by $-a/3$ along the *a* axis. As a consequence, any pair of 3n and 3(n+1) layers coincide in projection on the *ab*-plane (Fig. 15a) if layers are numbered within a NaBu crystal. Thus, the energy necessary for the NaBu-to-HBi structural transformation is minimized if the 1H phase results from the displacement of (3n+1) and (3n+2) layers by $+a/3$ and $-a/3$, respectively, along the *a* axis (Fig. 15a). Similarly, the 1M structure, in which adjacent layers are shifted by $+a/3$ along the *a* axis, may be obtained from the displacement of (3n+1) and (3n+2) layers by $-a/3$ and $+a/3$, respectively, along the *a* axis (Fig. 15b).

However, the reaction may start simultaneously from different parts of a crystal, resulting in the presence of stacking faults. The formation of a 1M layer pair (stacking fault) in the 1H phase is shown in Figure 15c where the arrowed layer 3(n+1)+1 is shifted by $-a/3$, instead of $+a/3$ in the ideal case, along the *a* axis. As a result this layer forms an hexagonal layer pair with the adjacent layer 3m. As mentioned previously, the amount of stacking faults is likely to depend on the reaction rate. At pH 5, the layer stacking is controlled mainly by the crystal-chemical features of NaBu (interlayer charge and proportion of Mn^{4+}_{layer}), rather than by the physico-chemical conditions (amount of available protons). Furthermore, the reaction is rather slow, and defective stacking of adjacent layers may be modified by additional layer displacements ($\pm a/3$). Accordingly, at pH 5 the structural alteration of NaBu leads to the formation of almost periodic 1H and 1M phases containing few well-defined stacking faults (Table 4). At pH 4, the reaction rate significantly increases and, as a result, stacking faults are "frozen" in the transformation products of both NaBu modifications, with 1H and 1M phases containing an increased proportion of well-defined stacking faults (Table 4). Due to the high proportion of these stacking faults, the relative abundances of 1M (40%) and 1H (60%) phases differ from the relative proportions of Nabu type I (20%) and II (80%). At lower pH values, the structural control due to the crystal-chemical features of NaBu modifications is less influential, the pH being the overwhelming driving force for the transformation. As a consequence, hydrogen bonding takes the dominant role in the layer stacking mode, finally resulting in the formation of a unique, and almost defect-free, 1H phase at pH 2.

Mechanism of NaBu-to-HBi conversion

From the simulation of the XRD patterns obtained for the four HBi samples it is possible to refine the NaBu-to-HBi conversion mechanism initially proposed by Silvester et al. (1997), that is the direct migration of Mn^{3+}_{layer} to the interlayer (2/6 cations × 1/3 rows = 0.111) and the adsorption of Mn^{2+} from solution into interlayers. The presence of Mn^{2+} in solution resulted from the initial rapid disproportionation of 0.111 Mn^{3+}_{layer} resulting in 0.055 Mn^{4+}_{layer} and 0.055 $Mn^{2+}_{solution}$. Prior to the re-adsorption of Mn^{2+}, the 0.055 Mn^{2+} measured in solution is constant over the pH range 2-5 (Silvester et al. 1997). In the subsequent slow equilibration phase, Mn^{2+} re-adsorbs from solution onto vacant layer sites to an extent dependent upon the solution pH. At pH 5 all solution Mn^{2+} re-adsorbs, whereas no re-adsorption occurs at pH 2. According to this model, the amount of $Mn_{interlayer}$ decreases from 0.167 (0.111 + 0.055; pH 5) to 0.111 (0.111 + 0; pH 2) atoms per octahedron, whereas the number of layer vacancies is invariant and equal to 0.167.

Here, the predicted amount of vacant layer sites was confirmed by the simulation of the experimental XRD patterns for all studied samples. However, the amount of $Mn_{interlayer}$ in the four samples was found to be equal to 0.167 cation per octahedron. Thus, an additional source of Mn is needed to account

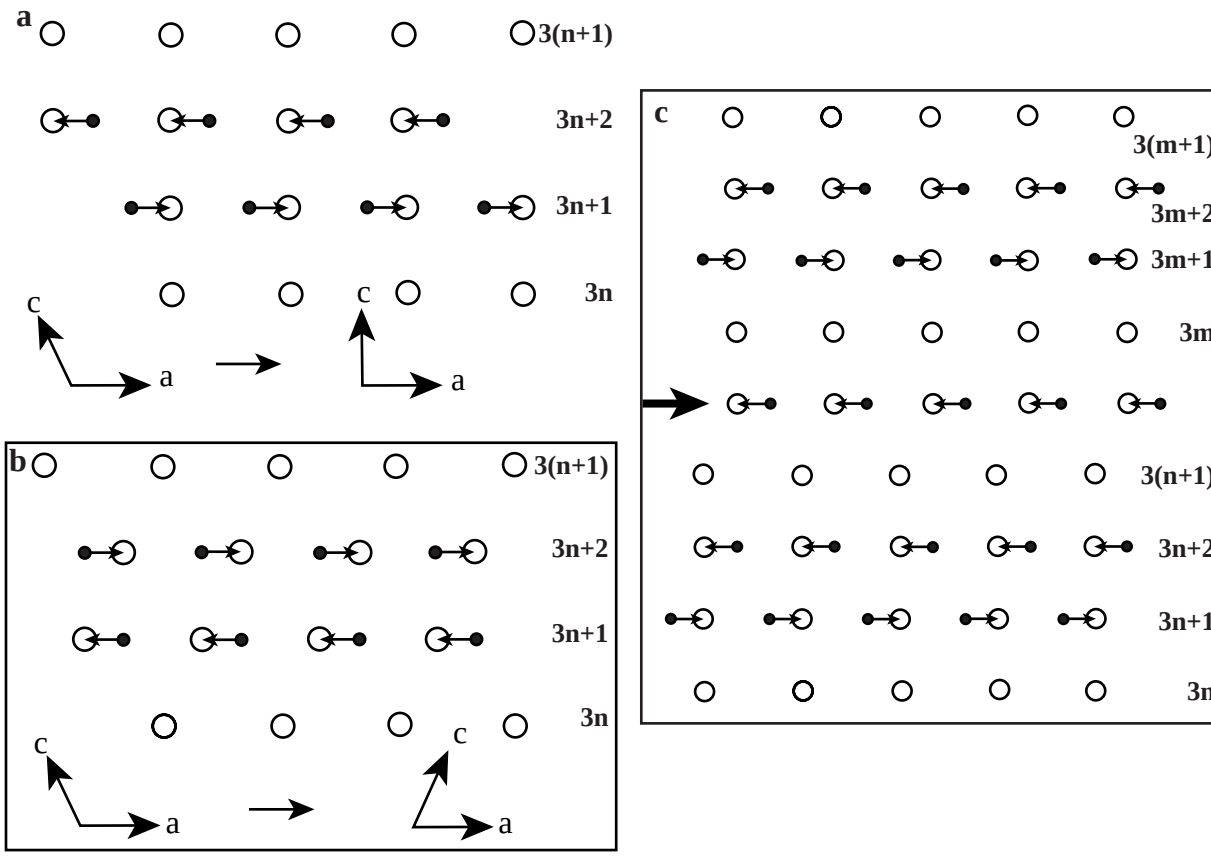

FIGURE 15. Schematic projection on the *ac*-plane of the mutual displacement of adjacent layers necessary to transform the initial NaBu stacking sequence, in which adjacent layers are shifted with respect to each other by $-a/3$ along the *a* axis, into the different HBi stacking sequences. Octahedral sites of HBi are shown as large open circles, whereas Mn_{layer} cations of NaBu are shown as small solid circles. Displacements of one layer with respect to the other are shown as arrows. (**a**) Fomation of 1H HBi, resulting from the displacement of (3n + 1) and (3n + 2) layers by $+a/3$ and $-a/3$, respectively, along the *a* axis. (**b**) Fomation of 1M HBi, resulting from the displacement of (3n + 1) and (3n + 2) layers by $-a/3$ and $+a/3$, respectively, along the *a* axis. (**c**) Fomation of well-defined 1M stacking faults in the 1H phase (large arrow). This stacking fault is obtained by shifting the arrowed layer 3(n + 1) + 1 by $-a/3$, instead of $+a/3$ in the ideal case, along the *a* axis. As a result this layer forms an monoclinic layer pair with the adjacent layer 3(n + 1).

for the constant $Mn_{interlayer}$ content, while still allowing for the incomplete re-adsorption of Mn^{2+} from solution at pH < 5 as measured by Silvester et al. (1997). The presence of a broad diffraction maxima in the XRD pattern of HBi pH 2 provides indirect evidence for the partial dissolution of NaBu with the lowering of pH. Possibly, the additional $Mn_{interlayer}$ originates from this partial dissolution because of the resulting re-adsorption of $Mn_{solution}$ into HBi interlayers, in parallel to the precipitation of a poorly crystallized phase.

Structural formulae of HBi prepared at different pH

If the assumption concerning the valency of additionally adsorbed Mn cations (i.e., Mn^{3+}) is valid, then one may calculate approximate structural formulae as a function of pH for HBi crystals resulting from the transformation of NaBu type II. As shown by Silvester et al. (1997), the fraction of Mn^{2+} re-adsorbed after the disproportionation stage is equal to 100% at pH 5, 77% at pH 4, 42% at pH 3, and 0% at pH 2. As shown earlier the structural formula of the 1H phase at pH 5 is $H^{+}_{0.33}Mn^{3+}_{0.111}Mn^{2+}_{0.055}(Mn^{4+}_{0.722}Mn^{3+}_{0.11}\square_{0.167})O_2\cdot(H_2O)_{0.50}$. At pH 2 this phase should contain only Mn^{3+} and the structural formula of the crystals originating from NaBu type II should be $H^{+}_{0.33}Mn^{3+}_{0.167}(Mn^{4+}_{0.722}Mn^{3+}_{0.111}\square_{0.167})O_2(OH)^{-}_{0.055}\cdot(H_2O)_{0.445}$. In agreement with XRD results, dissolution does not influence the layer structure of the 1H phase, and the structural formulae of HBi at pH 4 and 3 may be derived from the amount of re-adsorbed Mn^{2+}: $H^{+}_{0.33}Mn^{3+}_{0.123}Mn^{2+}_{0.043}(Mn^{4+}_{0.722}Mn^{3+}_{0.111}\square_{0.167})O_2(OH)^{-}_{0.013}\cdot(H_2O)_{0.487}$ and $H^{+}_{0.33}Mn^{3+}_{0.143}Mn^{2+}_{0.023}(Mn^{4+}_{0.722}Mn^{3+}_{0.111}\square_{0.167})O_2(OH)^{-}_{0.033}\cdot(H_2O)_{0.467}$, respectively.

The origin of the *a* and *b* parameter variations

As mentioned previously, interlayer Mn cations are located either above or below vacant layer sites. The electrostatic interaction between an interlayer Mn cation and the six nearest Mn_{layer} cations depends on the valency of these cations. For the same layer cation composition, the replacement of one interlayer Mn^{2+} cation by one Mn^{3+} cation significantly increases the repulsion between these species. To screen this effect, basal O

atoms forming the triangular basis of interlayer Mn octahedra should move toward each other in the *ab*-plane. The higher the amount of interlayer Mn^{3+}, the higher the amplitude of this displacement and, as a consequence, the smaller the *a* and *b* parameters should be. Of course the absolute change of these parameters should remain very small as observed experimentally (Table 1).

ACKNOWLEDGMENTS

The authors thank Pr. Alain Plançon (University of Orléans) for providing us with a copy of his simulation program. We are also grateful to H. Stanjek and to J. Post for their constructive reviews, and to Tony Eggleton for his editorial assistance. VAD is grateful to the Russian Science Foundation for financial support. BL acknowledges financial support from the INSU/CNRS "Géomatériaux" program.

REFERENCES CITED

Bach, S., Henry, M., Baffier, N., and Livage, J. (1990) Sol-gel synthesis of manganese oxides. Journal of Solid State Chemistry, 88, 325–333.

Bricker, O. (1965) Some stability relations in system $Mn-O_2-H_2O$ at 25 °C and one atmosphere total pressure. American Mineralogist, 50, 1296–1354.

Brown, I.D. (1981) The bond-valence method: An empirical approach to chemical structure and bonding. In M. O'Keefe, and A. Navrotsky, Eds., Structures and bondings in crystals II, vol. 2, p. 1–30. Academic Press, New York.

Brown, I.D. (1992) Chemical and steric constraints in inorganic solids. Acta Crystallographica, B48, 553–572.

Burns, R.G. and Burns, V.M. (1977) The mineralogy and crystal chemistry of deep-sea manganese nodules, a polymetallic resource of the twenty-first century. Philosophical Transactions of the Royal Society of London (A), 286, 283–301.

Burns, V.M. and Burns, R.G. (1978) Post-depositional metal enrichment processes inside manganese nodules from the north equatorial Pacific. Earth and Planetary Science Letters, 39, 341–348.

Chen, R., Chirayil, T., Zavalij, P., and Whittingham, M.S. (1996) The hydrothermal synthesis of sodium manganese oxide and a lithium vanadium oxide. Solid State Ionics, 68-88, 1–7.

Ching, S., Landrigan, J.A., Jorgensen, M.L., Duan, N., Suib, S.L., and O'Young, C.L. (1995) Sol-Gel synthesis of birnessite from $KMnO_4$ and simple sugars. Chemistry of Materials, 7, 1604–1606.

Chukhrov, F.V., Gorschkov, A.I., Rudnitskaya, E.S., and Sivtsov, A.V. (1978) Birnessite characterization. Investiya Akademie Nauk, SSSR, Seriya Geologicheskaya, 9, 67–76.

Chukhrov, F.V., Sakharov, B.A., Gorshkov, A.I., Drits, V.A., and Dikov, Yu.P. (1985) Crystal structure of birnessite from the Pacific Ocean. International Geology Review, 27, 1082–1088 (translated from Investiya Akademie Nauk, SSSR, Seriya Geologicheskaya, 8, 66–73).

Chukhrov, F.V., Gorshkov, A.I., and Drits, V.A. (1989) Supergenic manganese hydrous oxides, 208 p. Nauka, Moscow.

Cornell, R.M. and Giovanoli, R. (1988) Transformation of hausmannite into birnessite in alkaline media. Clays and Clay Minerals, 36, 249–257.

Drits, V.A. and McCarty, D. (1996) A simple technique for a semi-quantitative determination of the trans-vacant and cis-vacant 2:1 layer contents in illites and illite-smectites. American Mineralogist, 81, 852–863.

Drits, V.A. and Tchoubar, C., with the collaboration of Besson, G., Bookin, A.S., Rousseaux, F., Sakharov, B.A., and Tchoubar, D. (1990) X-ray diffraction by disordered lamellar structures: Theory and applications to microdivided silicates and carbons, 371 p. Springer-Verlag, Berlin.

Drits, V.A., Silvester, E., Gorshkov, A.I., and Manceau, A. (1997a) The structure of monoclinic Na-rich birnessite and hexagonal birnessite. Part 1. Results from X-ray diffraction and selected area electron diffraction. American Mineralogist, 82, 946–961.

Drits, V.A., Lanson, B., Gorskhov, A.I., and Manceau, A. (1997b) Determination of the content and distribution of fixed ammonium in illite-smectite by X-ray diffraction: Application to North Sea illite-smectite. American Mineralogist, 82, 79–87.

Drits, V.A., Lanson, B., Gorskhov, A.I., and Manceau, A. (1998) Sub- and superstructure of four-layer Ca-exchanged birnessite. American Mineralogist, 83, 97–118.

Giovanoli, R., Stähli, E., and Feitknecht, W. (1970a) Über Oxidhydroxide des vierwertigen Mangans mit Schichtengitter. 1. Mitteilung: Natriummangan(II,III) manganat(IV). Helvetica Chimica Acta, 53, 209–220.

Giovanoli, R., Stähli, E., and Feitknecht, W. (1970b) Über Oxidhydroxide des vierwertigen Mangans mit Schichtengitter. 2. Mitteilung: Mangan(III)-manganat(IV). Helvetica Chimica Acta, 53, 453–464.

Giovanoli, R., Feitknecht, W., Maurer, R., and Häni, H. (1976) Homogene Keimbildung und Keimwachstum von γMnO_2. Chimia, 30, 268–269.

Glover, E.D. (1977) Characterization of a marine birnessite. American Mineralogist, 62, 278–285.

Guinier, A. (1964) Théorie et technique de la radiocristallographie, 740 p. Dunod, Paris.

Kodama, H., Gatineau, L., and Méring, J. (1971) An analysis of X-ray diffraction line profiles of microcrystalline muscovites. Clays and Clay Minerals, 19, 405–413.

Kuma, K., Usui, A., Paplawsky, W., Gedulin, B., and Arrhenius, G. (1994) Crystal structures of synthetic 7 Å and 10 Å manganates substituted by mono- and divalent cations. The Mineralogical Magazine, 58, 425–447.

Manceau, A. and Charlet, L. (1992) X-ray absorption spectroscopic study of the sorption of Cr(III) at the oxide-water interface. Journal of Colloid and Interface Science, 148, 425–442.

Manceau, A., Gorshov, A.I., and Drits, V.A. (1992) Structural chemistry of Mn, Fe, Co and Ni in manganese hydrous oxides: Part II. Information from EXAFS spectroscopy and electron and X-ray diffraction. American Mineralogist, 77, 1144–1157.

Manceau, A., Drits, V.A., Silvester, E., Bartoli, C., and Lanson, B. (1997) Structural mechanism of Co^{2+} oxidation by the phyllomanganate buserite. American Mineralogist, 82, 1150–1175.

McKenzie, R.M. (1967) The sorption of cobalt by manganese minerals in soils. Australian Journal of Soil Research, 5, 235–246.

Murray, J.W. (1974) The surface chemistry of hydrous manganese dioxide. Journal of Colloid and Interface Science, 46, 357–371.

Post, J.E. and Appleman, D.E. (1988) Chalcophanite, $ZnMn_3O_{7.3}H_2O$: New crystal structure determinations. American Mineralogist, 73, 1401–1404.

Post, J.E., and Veblen, D.R. (1990) Crystal structure determinations of synthetic sodium, magnesium, and potassium birnessite using TEM and the Rietveld method. American Mineralogist, 75, 477–489.

Reynolds, R.C. Jr (1989) Diffraction by small and disordered crystals. In Mineralogical Society of America Reviews in Mineralogy, 20, 145–181.

Silvester, E.J., Charlet, L., and Manceau, A. (1995) The mechanism of Cr(III) oxidation by Na-buserite. Journal of Physical Chemistry, 99, 16662–16669.

Silvester, E., Manceau, A., and Drits, V.A. (1997) The structure of monoclinic Na-rich birnessite and hexagonal birnessite. Part 2. Results from Chemical Studies and EXAFS Spectroscopy. American Mineralogist, 82, 962–978.

Stone, A.T. (1987) Reductive dissolution of manganese (III,IV) oxides by substituted phenols. Environmental Science and Technology, 21, 979–988.

Stone, A.T. and Morgan, J.J. (1984) Reductive dissolution of manganese (III) and manganese (IV) oxides by organics. Environmental Science and Technology, 18, 617–624.

Stone, A.T. and Ulrich, H.J. (1989) Kinetics and reaction stoichiometry in the reductive dissolution of manganese(IV) dioxide and Co(III) oxide by hydroquinone. Journal of Colloid and Interface Science, 132, 509–522.

Strobel, P., Charenton, J.C., and Lenglet, M. (1987) Stuctural chemistry of phyllomanganates: Experimental evidence and structural models. Revue de Chimie Minérale, 24, 199–220.

Stumm, W. (1992) Chemistry of the solid-water interface: Processes at the mineral-water and particle-water interface in natural systems, 428 p. Wiley, New York.

Wehrli, B., Friedl, G., and Manceau, A. (1995) Reaction rates and products of manganese oxidation at the sediment-water interface. In C.P. Huang, C. O'Melia, and J.J. Morgan, Eds., Advances in Chemistry Series No. 244, Aquatic Chemistry: Principles and Applications of Interfacial and Inter-Species Interactions in Aquatic Systems, p. 111–134. American Chemical Society of America, Washington.

MANUSCRIPT RECEIVED SEPTEMBER 28, 1998
MANUSCRIPT ACCEPTED DECEMBER 23, 1999
PAPER HANDLED BY R.A. EGGLETON